Formation of plasma channels in the interaction of a nanosecond laser pulse at moderate intensities with helium gas jets

E. De Wispelaere,[1] V. Malka,[1] S. Hüller,[2] F. Amiranoff,[1] S. Baton,[1] R. Bonadio,[1] M. Casanova,[3] F. Dorchies,[1] R. Haroutunian,[1] and A. Modena[4]

[1]*Laboratoire pour l'Utilisation des Lasers Intenses, Unité mixte No. 7605, CNRS-CEA-Ecole, Polytechnique-Université Pierre et Marie Curie, Ecole Polytechnique, 91128 Palaiseau Cedex, France*

[2]*Centre de Physique Théorique, Centre National de la Recherche Scientifique, Ecole Polytechnique, 91128 Palaiseau Cedex, France*

[3]*Commissariat à l'Energie Atomique, Bruyères-le-Châtel, Boîte Postale 12, 91680 Bruyères-le-Châtel, France*

[4]*Imperial College, London, United Kingdom*

(Received 26 August 1998; revised manuscript received 28 January 1999)

We report on a detailed study of channel formation in the interaction of a nanosecond laser pulse with a He gas jet. A complete set of diagnostics is used in order to characterize the plasma precisely. The evolution of the plasma radius and of the electron density and temperature are measured by Thomson scattering, Schlieren imaging, and Mach-Zehnder interferometry. In gas jets, one observes the formation of a channel with a deep density depletion on axis. Because of ionization-induced defocusing which increases the size of the focal spot and decreases the maximum laser intensity, no channel is observed in the case of a gas-filled chamber. The results obtained in various gas-jet and laser conditions show that the channel radius, as well as the density along the propagation axis, can be adjusted by changing the laser energy and gas-jet pressure. This is a crucial issue when one wants to adapt the channel parameters in order to guide a subsequent high-intensity laser pulse. The experimental results and their comparison with one-dimensional (1D) and two-dimensional hydrodynamic simulations show that the main mechanism for channel formation is the hydrodynamic evolution behind a supersonic electron heat wave propagating radially in the plasma. It is also shown from 2D simulations that a fraction of the long pulse can be self-guided in the channel it creates. The preliminary results and analyses on this subject have been published before [V. Malka *et al.*, Phys. Rev. Lett. **79**, 2979 (1997)].
[S1063-651X(99)06206-6]

PACS number(s): 52.40.Nk, 52.50.Jm

I. INTRODUCTION

Applications of ultraintense laser-matter interaction physics such as laser-driven electron acceleration [1–3], x-ray lasers [4], high harmonic generation [5], or inertial confinement fusion [6], usually require that a high-intensity laser pulse propagate over a long distance. To achieve this, the laser beam has to overcome natural diffraction, characterized by the so-called Rayleigh length.

Various mechanisms have been considered to increase the interaction length. Milchberg *et al.* created plasma channels by focusing a 100 ps laser pulse (5 GW) into a gas-filled chamber with an axicon lens. The formation of a radial shock wave at the plasma-gas interface results in a fiberlike density profile. The density profile in this case was uniform along the laser axis, but the plasma was not fully ionized [7]. An incomplete ionization of the interacting plasma can be of great importance when considering refraction effects [8]. Nevertheless, the guiding of a ''low-intensity'' beam ($10^{14}\,\mathrm{W/cm^2}$) in these channels has been demonstrated [9,10] over 70 Rayleigh lengths (2.2 cm) and a $5\times10^{15}\,\mathrm{W/cm^2}$ pulse has been guided over 1 cm with a transmitted energy of 30%. In the past few years, relativistic and ponderomotive self-channeling have been realized by several teams [11–13]. These mechanisms provide a way to generate a guiding structure during the laser pulse itself. More recently, Krushelnick *et al.* [14] have demonstrated the guiding of an intense pulse ($I>5\times10^{16}\,\mathrm{W/cm^2}$) injected into a ponderomotively driven plasma waveguide generated by a 2 TW laser beam ($I>10^{18}\,\mathrm{W/cm^2}$) in a hydrogen gas jet. No direct measurements of the radial and longitudinal density profiles were performed in these experiments. A very different technique used by Ehrlich *et al.* [15] consists in forming the plasma channel by a slow capillary discharge. The guiding of a $10^{16}\,\mathrm{W/cm^2}$ laser pulse over 10 Rayleigh lengths (1 cm) has been demonstrated under these conditions, but the plasma was not fully ionized and the electron density could not be decreased below $10^{19}\,\mathrm{cm^{-3}}$. Guiding of terawatt laser pulses by hollow capillary tubes has also been tested by several groups [16,17] through measurements of transmitted laser energy.

In this paper, we present detailed results on the experimental realization of fully ionized plasma channels. These channels are obtained by focusing a 600 ps laser beam at moderate intensity (10^{13}–$10^{15}\,\mathrm{W/cm^2}$) on the edge of a helium gas jet. This study demonstrates that the use of a gas jet is a way to avoid both ionization-induced refraction of the guided intense pulse [18] and refraction of the channel-producing pulse. Our results show that the electron density is depleted along the laser axis over the whole length of the gas jet (2.5 mm) and that the electron density can be adjusted by changing the laser energy and gas pressure. In order to demonstrate the importance of refraction effects, we also investigated the density evolution by focusing the laser beam in a gas-filled chamber. We show that the helium gas is fully ionized, but that refraction strongly modifies the plasma ex-

 ©1999 The American Physical Society

pansion compared to the gas-jet case, leading to the absence of any useful channel. These studies have been performed with a complete set of diagnostics such as Thomson scattering, stimulated Raman backscattering, Schlieren imaging, and interferometry. These diagnostics give us information on the electron temperature and evolution of the electron density profile. Preliminary results on gas jets and their comparison with 1D simulations are presented in Ref. [19]. Additional results are presented on the interaction in a gas-filled chamber, as well as on the channel formation and measurement of the plasma parameters in various laser and gas-jet conditions. Two-dimensional simulations also show that part of the ionizing beam is guided in the evolving channel.

The paper is organized as follows: The experimental setup is presented in Sec. II. Section III is devoted to the experimental results. The case of focusing in a gas-filled chamber is compared with the case of a gas jet. We then discuss, in Sec. IV, physical processes that contribute to the formation of the plasma channel in the gas jet. Experimental results are compared with simulations using 1D and 2D codes. In Sec. V, we summarize and discuss the main experimental results and outline the perspectives.

II. EXPERIMENTAL SETUP

The experiments were performed at the Laboratoire pour l'Utilisation des Lasers Intenses (LULI) with an infrared ($\lambda_L = 1.053\,\mu$m) neodymium-glass laser beam, linearly polarized and frequency doubled to 0.526 μm with a maximum energy of 25 J on target. The pulse duration was 600 ps full width at half maximum (FWHM) with a Gaussian shape. The 90-mm-diam laser beam was focused with an $f/3$ doublet lens to a 28-μm-diam focal spot (FWHM) (7 times the diffraction limit of a perfect Gaussian beam), and the intensity in vacuum reached $5\times10^{15}\,\mathrm{W/cm^2}$. The experimental Rayleigh length, defined as the length over which the maximum intensity decreases by a factor of 2, is measured to be about 250 μm. The laser beam was focused either in a gas-filled chamber or on a pulsed helium supersonic gas jet (Mach 4-5). The gas jet is produced by means of a fast operating valve and a convergent-divergent Laval nozzle. The rise time (1 ms) of the fast valve and the duration of the gas puff (2–3 ms) were measured using Schlieren techniques. At 1 mm under the exit of the cylindrical nozzle, which has an inner diameter of 2.5 mm, the neutral density in the center can be adjusted between 10^{18} and $3\times10^{19}\,\mathrm{atoms\,cm^{-3}}$. In the higher-density case, the density gradient at the edge of the jet is $\Delta n_{\mathrm{at}} = 2.5\times10^{19}\,\mathrm{atoms/cm^3}$ over 450 μm.

To obtain interferograms and Schlieren images, a 600 ps collimated probe beam at 0.526 μm propagates through the plasma at 90° to the interaction beam (see Fig. 1). All Mach-Zehnder interferograms presented in this paper correspond to time-integrated images of the plasma, recorded 530 ps after the interaction beam (i.e., the delay between the peaks of the pump beam and the probe beam is 530 ps). As we will see subsequently, the plasma expansion at this time is sufficiently slow to obtain in most cases well-defined fringes during the 600 ps probe beam duration. In order to measure the evolution of the plasma parameters (electron density and electron temperature), self-emitted Thomson scattering is collected with an $f/2.5$ achromatic lens at 45° from the incident laser beam and resolved both temporally and spectrally by a spectrometer-streak camera system. In addition to these parameter measurements, a similar system is used to obtain the time-resolved Raman-backscattered spectra.

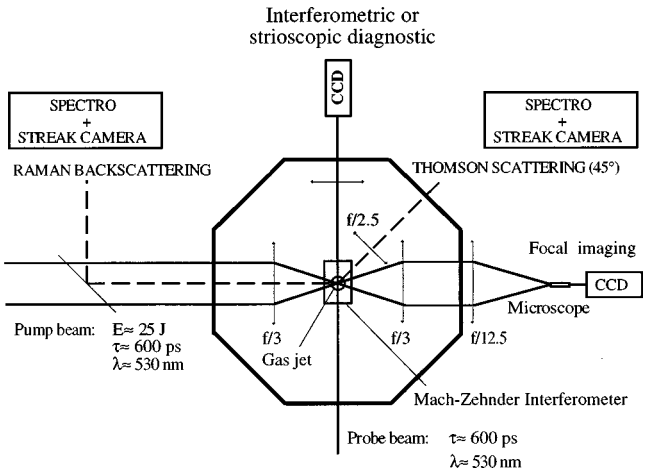

FIG. 1. Experimental set-up

III. EXPERIMENTAL RESULTS

In the following section we describe the experimental results obtained in the gas-filled chamber (Sec. III A) and in the gas jet (Sec. III B). The gas-filled chamber experiments are presented to outline the defocusing effects on the interaction beam induced by ionization. This effect does not allow the formation of a plasma channel. In Sec. III B, the results are compared with gas-jet experiments, where the channel can be easily produced. The optimization of this channel is discussed in Sec. III C.

A. Gas-filled chamber experiments

The interferogram in Fig. 2 corresponds to a plasma resulting from the focusing of a laser pulse in a gas-filled chamber. In order to keep a sufficient radial resolution, three different interferograms have been taken at different positions along the plasma. The helium pressure is 760 Torr, and the plasma is produced over a 6 mm length and a 900 μm width. The filamentary structures seen at the right of the interferogram are probably due to the presence of hot spots in the laser beam. They are also present in the middle of the plasma, so that it is not possible to assume the cylindrical symmetry necessary to deduce the radial electron density profile via Abel inversion.

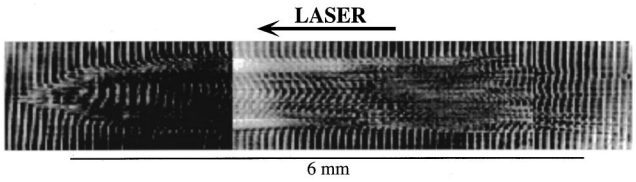

FIG. 2. Time-integrated interferograms of the plasma produced in the chamber filled with helium gas ($P = 760$ Torr, full energy shot $E = 25$ J).

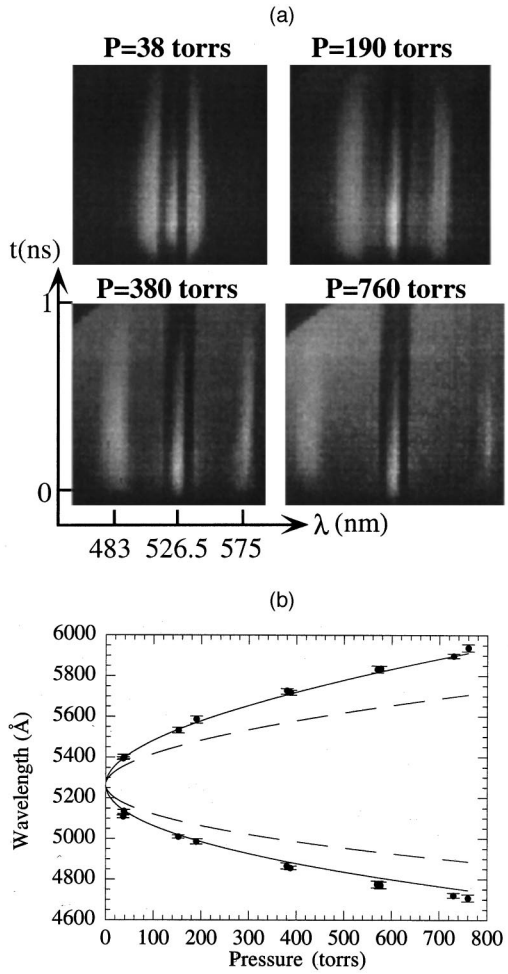

FIG. 3. (a) Time-resolved Thomson-scattering spectra at 45° to the laser axis for different helium pressures in the chamber ($E = 25$ J). The ion peak is attenuated by a factor of 100. (b) Wavelength of the electron satellite as a function of the pressure in the chamber. The theoretical positions corresponding to the first and second ionization states of helium are plotted, respectively, by dashed and solid lines.

To determine the evolution of the electron density, time-resolved Thomson scattering of the interaction beam was performed. Light is collected at 45° with respect to the laser axis and the slit of the streak camera limits the source radial size to 50 μm. In order to measure both the ion and electron features on a single shot, the ion peak was attenuated by a factor of 100 [Figs. 3(a) and 6].

Thomson-scattered spectra in the gas-filled chamber are presented for different values of the helium pressure in Fig. 3(a). The electron satellites are clearly visible on both sides of the ion peak according to the Bohm-Gross dispersion relation given by [20] $\omega=(\omega_p^2+3k^2v_t^2)^{1/2}$, where $\omega_p=(n_e e^2/m\varepsilon_0)^{1/2}$ is the electron plasma frequency, k is the electron plasma wave number (difference between the scattered wave number and the wave vector of the incident laser pulse k_0), and v_t is the electron thermal velocity. The wavelengths corresponding to the red and blue satellites of the electron spectra are plotted as a function of the gas pressure in Fig. 3(b). The lines correspond to the theoretical positions for the first and second ionization states neglecting the thermal correction in the Bohm-Gross frequency. It is obvious from this graph that the helium gas is indeed fully ionized. This was observed in all our experiments, even when the laser energy was decreased down to 1 J, which corresponds to a laser intensity in vacuum close to 10^{14} W/cm^2. As will be explained in Sec. IV, this is due to the fact that the heating is efficient enough to produce plasma temperatures high enough to reach the second ionization state of helium (at an energy of 54 eV). Looking at the temporal behavior of the electron satellites in Fig. 3(a), we see that the position of the satellites is constant in time, which means that the electron density does not change during the interaction time. It should be noted that the peak intensity of the electron satellites appears later in time when the pressure is decreased ($t_{\max}=100$ ps at 780 Torr against 350 ps at 380 Torr, with a time origin corresponding to the beginning of the satellite). It suggests that at higher pressures the creation of the plasma occurs near the maximum of the pulse. This is explained by the fact that the ionization-induced refraction reduces the peak laser intensity, this effect being more efficient at higher pressures. The next section on gas-jet experiments confirms this conclusion.

B. Gas-jet experiments

In order to observe the efficient propagation of an intense pulse in a plasma waveguide, the pulse to be guided should not be defocused by ionization-induced refraction before and after entering the plasma channel. The use of the gas jet prevents defocusing in front of the gas jet. However, to prevent refraction inside the channel, it is also essential that the gas be fully ionized. As shown here, this will be the case inside the gas jet.

To measure the radial electron density profiles as well as the density and temperature evolution, we performed, respectively, interferometric imaging of the plasma and Thomson self-scattering on electron and ion acoustic perturbations. Furthermore, to characterize the channel expansion, we have time-resolved the Schlieren imaging of the plasma. A time-resolved Raman backscattering measurement is also presented at the end of this section to provide an independent measure of the temperature.

An interferogram obtained when focusing the laser beam at full energy on the edge of the helium gas jet is shown in Fig. 4(a). As the plasma is generated about 500 ps before the maximum of the creation pulse, this interferogram gives us a radial electron density profile about 1.1 ns after its creation. In this picture the laser propagates from the right to the left. In the right part of the picture, we see the transition between unshifted fringes and fairly shifted fringes which indicate the plasma-vacuum boundary. The radial plasma size is about 300 μm in diameter, and the plasma covers the whole length (2.5 mm) of the gas jet. As the plasma diameter in the gas-filled chamber was 900 μm, this first indicates that self-defocusing of the laser beam is greatly reduced with the gas jet, as already shown by several teams [18,21]. The plasma length is limited by the dimension of the gas jet itself.

Assuming cylindrical symmetry, we can deduce the radial electron density profile from the interferogram via Abel inversion. A characteristic radial density profile is plotted in Fig. 4(b) for fringe No. 20 [cf. Fig. 4(a)]. In contrast to the case of the gas-filled chamber, where no electron density

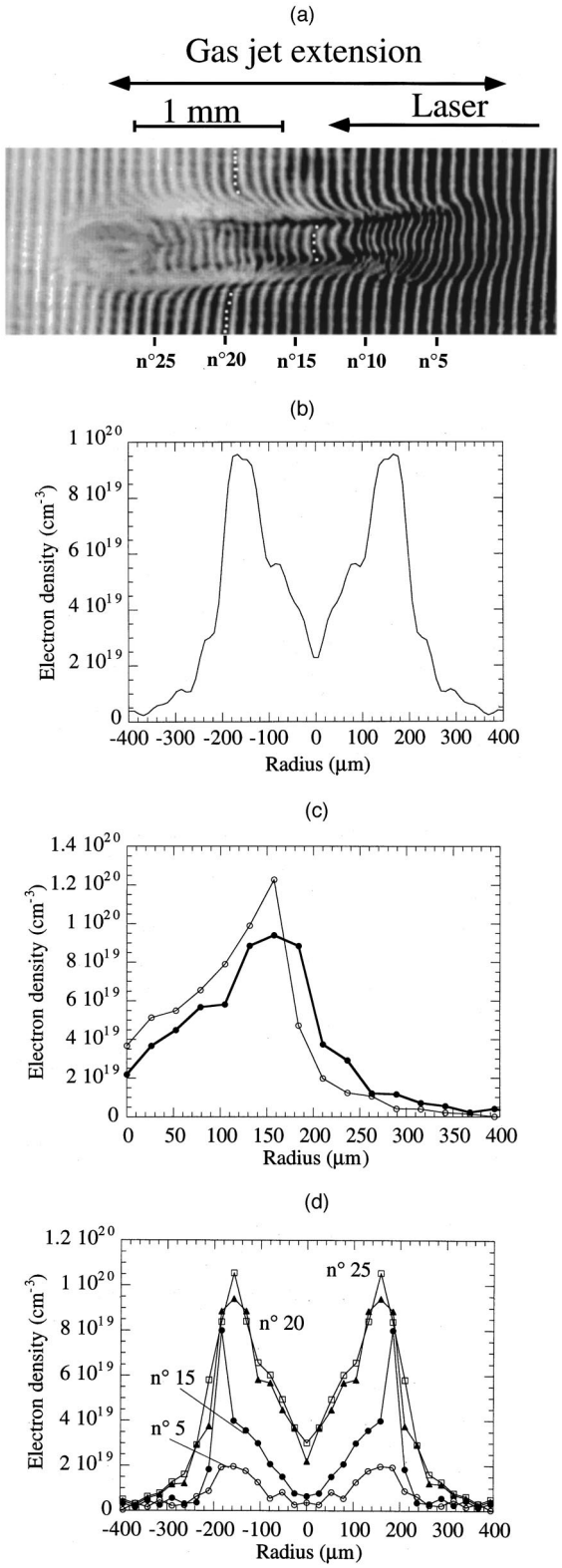

FIG. 4. (a) Time-integrated interferogram in the gas jet for a pulse energy $E=25\,\mathrm{J}$ ($I_{L\mathrm{vacuum}}=5\times10^{15}\,\mathrm{W/cm^2}$) and $n_{\mathrm{at}}\approx3\times10^{19}\,\mathrm{atoms/cm^3}$. The time delay between the pump and probe beams is 530 ps for all interferograms. (b) Electron density profile for fringe No. 20 marked with white dots in (a). (c) Electron density profiles deduced at a given point along the propagation axis from the upper and lower parts of the interferogram (fringe No. 20). (d) Electron density profiles deduced from fringes No. 5, 15, 20, and 25.

depletion could be measured, the profile presents a density minimum on axis. The electron density increases from $2\times10^{19}\,\mathrm{cm^{-3}}$ on axis to $9\times10^{19}\,\mathrm{cm^{-3}}$ at a radius of 160 μm, and the density difference is already higher than $10^{19}\,\mathrm{cm^{-3}}$ at a radius of 30 μm. The on-axis electron density deduced from this interferogram is in good agreement with the time-resolved measurements obtained by Thomson scattering and presented later in this section. The largest source of errors in the calculation of the density profile is a possible deviation from cylindrical symmetry. It is estimated by inverting separately the upper and lower parts of the fringes. This is shown in Fig. 4(c) for fringe No. 20. The relative precision on the minimum density is observed to be of the order of 50%. On the contrary and because of the large fringe shift, the uncertainty in the exact position of the fringe leads to a relatively small uncertainty in the calculated density. The duration of the probe beam is $\approx$600 ps; thus, it was not possible to measure precisely the density profile at earlier times. The electron density profiles measured along the propagation axis (fringes No. 5, 10, 15, 20, and 25) are presented in Fig. 4(d). It appears that, after the low-density region, the channel is formed all along the gas jet and that the density profile only slowly depends on the position inside the jet.

A time-resolved Schlieren diagnostic was used to determine the radial evolution of the plasma-gas interface. Figures 5(a) and 5(b) show time-integrated images of the plasma for two different delays between the pump and probe beams, respectively, -250 and $+250$ ps. By imaging the refracted probe rays on the slit of a streak camera, as shown in Fig. 5(b), we can resolve the radial plasma expansion in time. A typical result is shown in Fig. 5(c). Together with the expansion of the outer edge of the plasma, the first bell-like zone on the left, one can observe several emitting zones at later times. The physical origin of these refracting regions is not clearly understood. It could be due to the dynamics of the focusing laser pulse in the evolving density profile. From Fig. 5(c), we plot the radius of the outer edge of the plasma as a function of time in Fig. 5(d). We observe a rapid initial expansion which tends to saturate at longer times. The diameter of 500 μm at saturation is in rather good agreement with the interferometric measurements shown in Fig. 4(b), giving an external diameter between 400 and 600 μm.

A typical time-resolved Thomson scattering spectrum obtained in the gas jet is shown in Fig. 6(a). In contrast with spectra obtained in the gas-filled chamber [Fig. 3(a)], we observe in this case a convergence of the red and blue electron satellites as a function of time, which indicates a strong decrease of the electron density with time on the laser axis. This behavior has been observed at various positions along the gas jet. From the scattered intensity as a function of time and assuming that the maximum intensity is reached at the maximum of the laser pulse, we can also observe on these spectra [Fig. 6(b)] that a significant ionization takes place earlier in the pulse than in the case of a gas-filled chamber. This is in agreement with the strong defocusing occurring in the latter case, thus decreasing the laser intensity. The on-axis electron density is deduced from the wavelengths of the electron satellites which are clearly visible on both sides of the ion peak (always attenuated by a factor of 100) and are shifted by the Bohm-Gross frequency. The time evolution of the electron satellites indicates a strong decrease of the on-

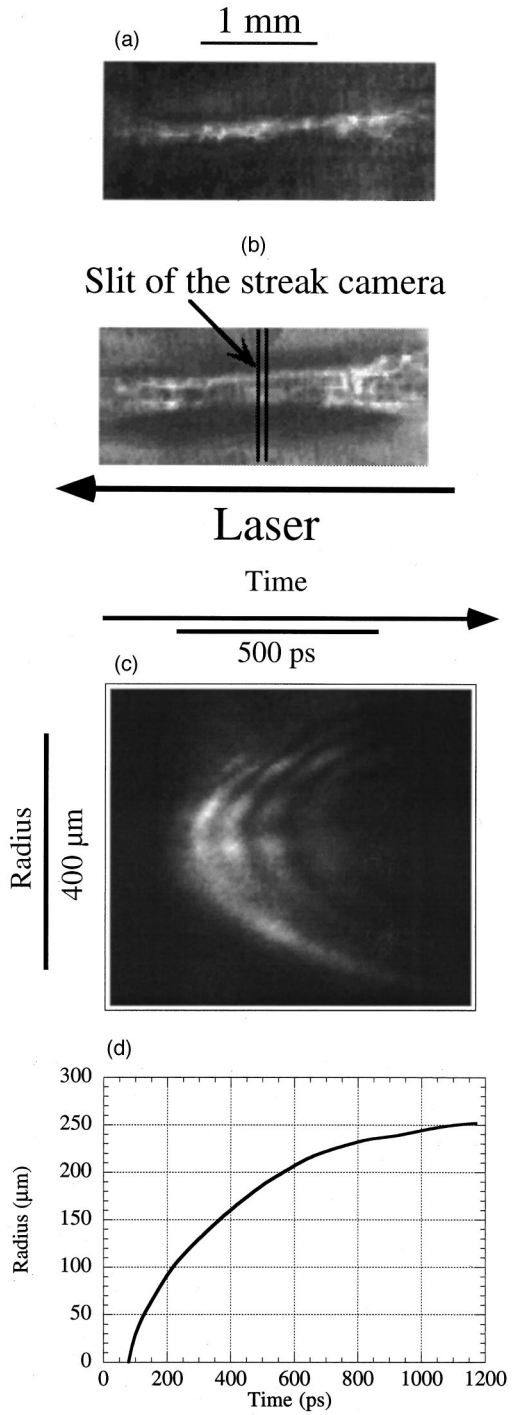

FIG. 5. (a) and (b) Time-integrated Schlieren images of the plasma produced in the gas jet ($E=25$ J, $n_{at}\approx 3\times 10^{19}$ atoms/cm^3) for two different delays between the probe and pump beams: (a) probe 250 ps before pump, (b) probe 250 ps after pump. (c) Time-resolved Schlieren images obtained by imaging the plasma on the slit of the streak camera as shown in (b). (d) Position of the gas-plasma interface as function of time.

axis electron density from 7×10^{19} to 2×10^{19} cm^{-3} during the interaction process.

Time-integrated but space-resolved spectra along the laser axis show full ionization of the plasma even in the vicinity of the gas-vacuum interface. This is shown in Fig. 7. The electron density deduced from the spectrum of Fig. 7(a) and

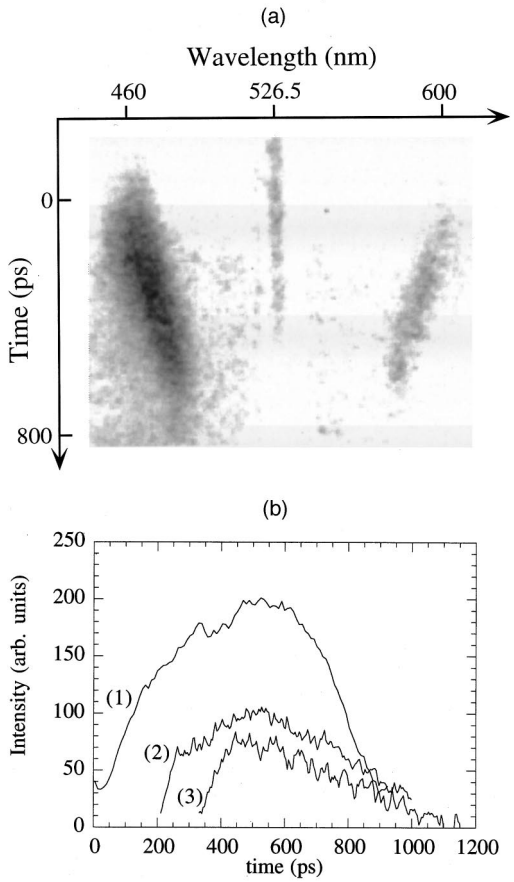

FIG. 6. (a) Time-resolved Thomson scattering spectra in the gas jet at 45° to the laser axis ($E=25$ J). (b) Spectrally integrated intensity in the electron satellite as function of time: (1) gas jet with $n_{at}\approx 3\times 10^{19}$ atoms/cm^3, (2) gas-filled chamber at 380 Torr ($n_{at}\approx 1.2\times 10^{19}$ atoms/cm^3), and (3) gas-filled chamber case at 760 Torr ($n_{at}\approx 2.4\times 10^{19}$ atoms/cm^3). In each case, the maximum of the signal is positioned at $t=530$ ps.

presented in Fig. 7(b) is in good agreement with the neutral density profile of the jet only if we assume a full ionization of the helium gas. As underlined in the preceding section, a full ionization of the gas is a crucial requirement if one wants to guide a subsequent high-intensity laser pulse.

The evolution of the electron temperature has been obtained by the analysis of electron and ion features of the Thomson scattering spectra. A typical ion feature is shown in Fig. 8(a). The scattered light is time resolved with a streak camera with a temporal resolution of 150 ps limited by the spectrometer (spectral resolution is 1.3 Å). The two satellites are separated by twice the ion acoustic frequency $\omega_{ia}=k_{io}c_s=f(T_e,T_i)$, where k_{io} is the ion wave vector and c_s is the ion acoustic velocity in the plasma. The shift of both satellites at the beginning of the signal is most probably due to the blueshift of the laser beam itself during the ionization phase. The distance between the two peaks as a function of time is plotted in Fig. 8(b). By fixing the ratio T_e/T_i, we can deduce an upper and a lower limit for the electron temperature as a function of time. It will be plotted with all other temperatures and compared with simulations in Sec. III.

A time-resolved measurement of Raman-backscattered spectra gives us independant information on the electron temperature. Raman spectra at three different pressures are

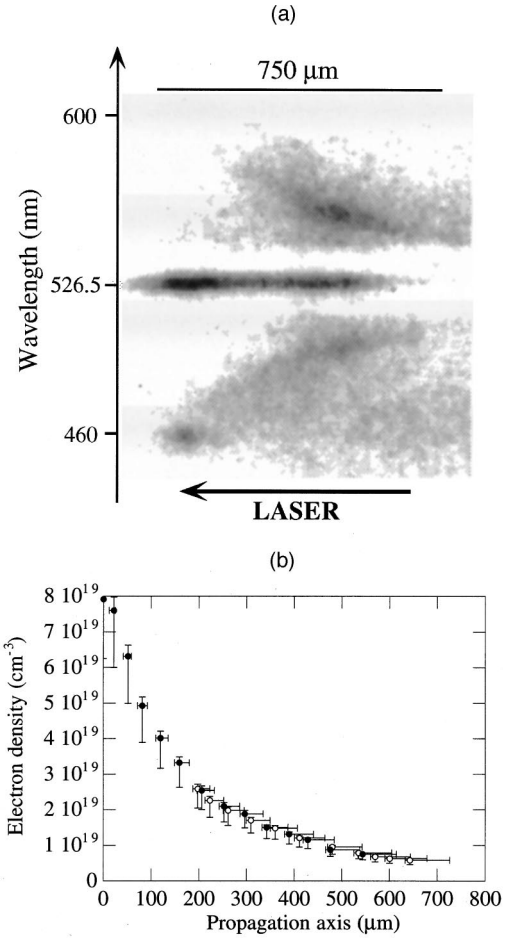

FIG. 7. (a) Space-resolved Thomson-scattering spectra near the edge of the gas jet ($E=25$ J, $n_{at}\approx 3\times 10^{19}$ atoms/cm^3). (b) Electron density deduced from (a) with the Bohm-Gross relation, neglecting the thermal correction. Dots, red satellite; circles, blue satellite.

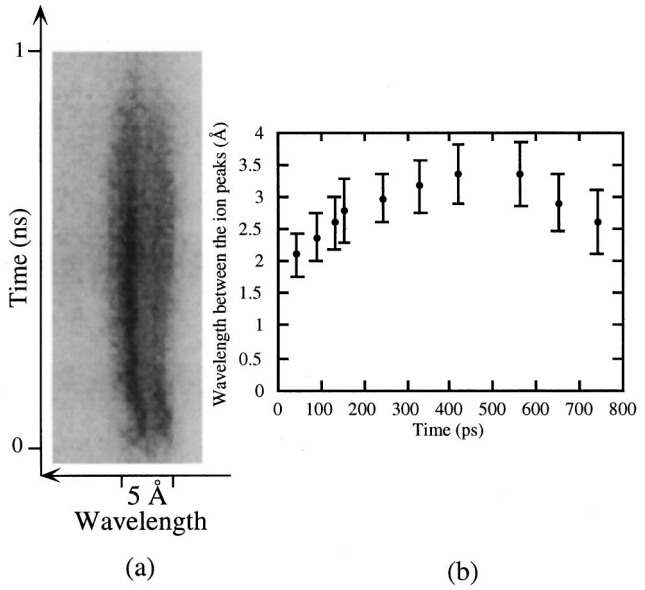

FIG. 8. (a) Time-resolved Thomson-scattering spectra on ion acoustic waves in the gas jet at 45° to the laser axis ($E=25$ J, $n_{at}\sim 3\times 10^{19}$ atoms/cm^3). (b) Separation between the ion peaks of Fig. 7(a) as a function of time.

presented in Fig. 9. We also show in this figure the Brillouin backscatter feature at the highest pressure. The total Brillouin reflectivity is of the order of 10%, whereas the Raman reflectivity is only of the order of 0.01%. On this spectra, we see that the Raman signal stops early in the laser pulse and that its duration does not exceed 250 ps. As a result of the plasma heating, the temperature increases, whereas the density decreases as a function of time. Landau damping of the electron plasma waves becomes dominant when $k_p\lambda_d\approx 0.3$ [20] ($k_p\approx 2k_0$ is the wave vector of the SRS driven plasma waves). We neglect here the effect of the laser field on the electron distribution function, which could slightly modify this criterion. However, this is not very important at our laser intensity, which stays most of the time below 10^{15} W/cm^2. From the position of the Raman cutoff in time (time $t=0$ corresponds to the beginning of the ion signal), we can deduce the value of the electron temperature at this time. These values are plotted in Fig. 9(d) and are in good agreement with the other diagnostics. It is clear from these results that the plasma heating is more rapid at higher densities, which is in agreement with collisional heating being the dominant absorption mechanism (see Sec. III).

C. Channel optimization

The formation of the channel and its evolution in time depend on the laser energy and gas-jet pressure. Thus the channel parameters can be modified by adjusting these last two parameters and by selecting the appropriate time delay after the gas-jet ionization. Experimentally, we observed the effect of the laser energy and of the gas atomic density.

The time evolution of the density near the laser axis is deduced from the Thomson scattering spectra. Spectra obtained at three different pressures and a laser energy of 2.5 J are shown in Figs. 10(a)–10(c). It is observed that the reduction in density between the initial density (measured at the beginning of the electron satellite) and the final density (at the end of the satellite) is independant of the initial density and is of 2.2–2.4. These on-axis electron densities are in relatively good agreement with the interferometric density profiles shown in Fig. 11. We emphasize here that, as already mentioned, the precision in the estimation of the on-axis electron density from Thomson-scattered spectra is better than from the interferograms themselves. We can see from Figs. 10 and 11 that by changing the initial backing pressure (or equivalently the initial neutral density) we can change the density profile and provide a channel with an adjustable axial density.

Thomson spectra at three different laser energies (24, 10, and 3 J) are shown in Figs. 10(d)–10(f). We can see from these spectra that the variation of the on-axis density is not affected by the decrease in laser energy. However, the radial evolution is slower at lower laser energy. An example of an interferogram at a laser energy of 3.5 J is shown in Fig. 12(a). The plasma is slightly shorter (1.8 mm) than at high energy and the radius (100 μm) is significantly smaller. The density profiles deduced from the interferograms are compared in Fig. 12(b). If the radius is smaller at low energy, the density difference (from minimum to maximum) remains comparable (5×10^{19} cm^{-3} compared to 7×10^{19} cm^{-3}).

Thus, by changing the laser energy and the atomic gas density, as well as the time delay after ionization, it seems possible to adjust the channel parameters to guide a laser

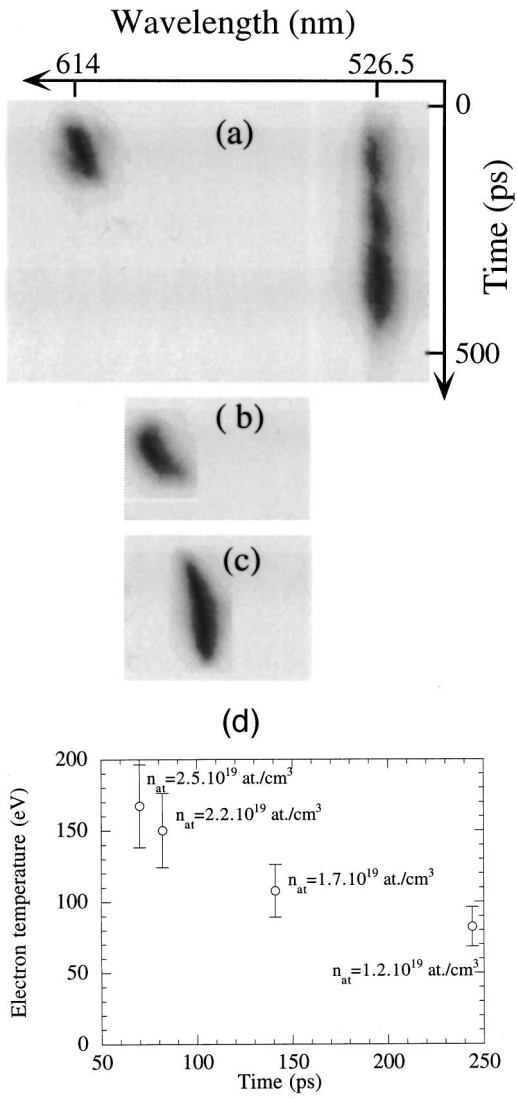

FIG. 9. (a)–(c) Time-resolved Raman and Brillouin backscattered spectra for three different gas-jet pressures: (a) $n_{at}=2.5\times10^{19}$ atoms/cm^3, (b) $n_{at}=1.7\times10^{19}$ atoms/cm^3, and (c) $n_{at}=1.2\times10^{19}$ atoms/cm^3. (d) Electron temperature deduced at the time of Raman Landau cut off for different gas-jet pressures (this is not a temperature evolution with time, but a single point for each shot).

beam with a given radius w_0, at a given density n_e, and with a required density difference between the axis and radius w_0 given by [9] $\Delta n_e = 1/r_0 \pi w_0^2$, where $r_0 \sim 2.82\times10^{-15}$ m is the classical electron radius, a given radius.

IV. ANALYSIS OF THE RESULTS AND PHYSICS OF CHANNEL FORMATION

A. Hydrodynamic simulations

In addition to the analysis of the experimental data, we used two different hydrodynamics codes to interpret the processes causing channel formation: the one-dimensional radiation hydrodynamics code MULTI [22] and the two-dimensional code FCI2 [23]. With MULTI we were able to study the radial hydrodynamic motion of the plasma around the laser axis close to the focal position. This code solves the hydrodynamic equations in Lagrangean coordinates, it includes electron heat transport, and it uses tabulated equation-of-state (EOS) data. Multigroup radiation transport, which is of minor importance in the present context, is also solved using tabulated opacity data. For the present purpose we used the version for cylindrical geometry. Since the cylinder axis $r=0$ corresponds to the laser propagation axis, laser energy deposition was imposed in a volume around $r=0$ using $\mathrm{div}\, S_z = dS_z/dz = -KS_z z(r)$ in the energy equation (where S_z stands for the laser flux and K for the absorption coefficient being proportional to the collisional frequency). In addition to MULTI, we used the 2D code FCI2 to compute the propagation of the beam inside the plasma with a 2D ray-tracing routine coupled to the hydrodynamic equations. FCI2 describes essentially the same physics as MULTI, however, on a coarser grid, with 400 ray trajectories. It allowed us to see beam trapping effects via its 2D-ray-tracing module.

Several physical mechanisms are not included in both codes.

(i) The fast dynamical evolution of field and tunnel ionization as well as effects beyond the validity of local thermal equilibrium (LTE) what concerns EOS and opacity data [24]. However, in the current context, ionization processes happen in the very early stage, say, within $t<100$ ps of the 600-ps-FWHM-long laser pulse. An exact description of ionization should include a calculation of the seeded avalanche breakdown initiated by multiphoton ionization. The laser intensity used in the experiment is high enough to produce direct multiphoton ionization of a fraction of the helium gas, which is then heated by collisional absorption. Subsequent ionization occurs through collisions, at a time which depends on the initial electron density, temperature, and neutral density. Characteristic times given by collisional ionization rates [25] vary from a few ps ($P\approx760$ Torr) up to 110 ps for the critical case of a neutral density of 10^{18} cm^{-3} with an electron temperature of 50 eV. Experimentally, the helium gas is fully ionized in the gas jet very early in the pulse frame, and even in the case of a gas-filled chamber at low pressure ($P\approx38$ Torr), the temperature is high enough to induce complete collisional ionization of helium. In the simulations with the codes, the fast ionization dynamics was therefore skipped and we assumed for simplicity from the beginning complete ionization of the He gas in the volume around $r=0$ where the laser intensity exceeded 10^{14} W/cm^2 (since the corresponding volume is larger than the volume where most of the laser deposition takes place, the simulation results prove not to be too sensitive with respect to this somewhat arbitrary choice of a threshold intensity).

(ii) Ponderomotive modifications and thus self-focusing are not taken into account self-consistently. In MULTI we simply assumed that the radial laser intensity profile keeps a Gaussian bell-like shape for the entire run. However, even for calculations that take into account self-focusing effects, the necessary information concerning the laser beam profile in amplitude and phase would be incomplete: the shape of the generic LULI laser beam is, as for most of the powerful laser beams, far from an ideal Gaussian laser beam. It is, on the other hand, quite evident that intense laser beams, which tend to self-guiding connected with purely ponderomotive channel formation, are trapped within a radius that is smaller than or of the same order as the focal radius of the entering laser beam. Under the current experimental conditions, this

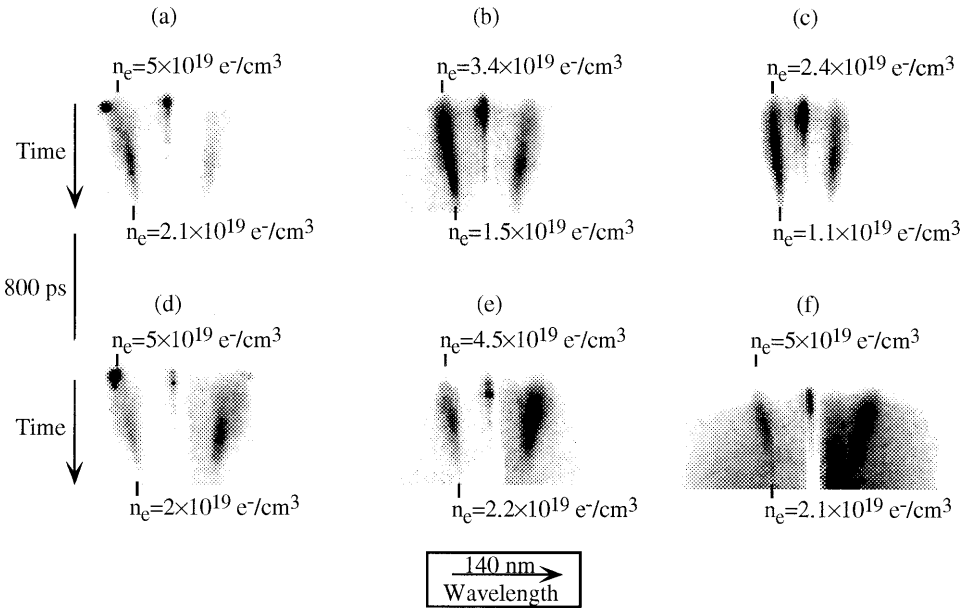

FIG. 10. Time-resolved Thomson-scattering spectra for three different gas-jet pressures (a) $n_{at}=2.5\times10^{19}$ atoms/cm^3, (b) $n_{at}=1.7\times10^{19}$ atoms/cm^3, and (c) $n_{at}=1.2\times10^{19}$ atoms/cm^3 and laser energies, (d) $E_L=24$ J, (e) $E_L=10$ J, and (f) $E_L=3$ J.

would correspond to radii of the order of $r<15-20\,\mu$m. Although ponderomotive self-focusing is certainly present, we stress that the observed radial evolution of the plasma and formation of a channel is beyond the corresponding radial dimensions. Thus the radial evolution of the plasma into the surrounding He gas for radii $r>20\,\mu$m is not governed by ponderomotive or thermal self-focusing effects.

B. Comparison of experimental data with numerical simulations

To take into account the possible ionization defocusing effect, the laser spot radius r_s was varied in the simulations. The comparison between the experimental and simulated evolution of the electron density on the laser axis is shown in Fig. 13. The experimental density is deduced from Fig. 6 for the two different shots. The small thermal correction in the Bohm-Gross relation has been taken into account to obtain the values shown in Fig. 13. (Temperature measurements are discussed in the next paragraph.) The error bars in n_e are mainly determined by the temperature uncertainty and do not include the spectral width of the satellite. In spite of the simplified description of the local laser profile in the simulation, which could induce a discrepancy in the temporal behavior, good agreement is obtained for a radius range between $r_s=1.5r_0$ and $2.3r_0$, where r_0 is the laser spot size measured in vacuum. The electron density drops from 6.5×10^{19} cm^{-3} down to about 2×10^{19} cm^{-3}, which is attained just after the laser pulse maximum. With a larger radius ($r_s=7.3r_0$), the predicted density evolution is much too slow to fit the experimental data. However, with a radius close to $2.3r_0$, a change of the laser energy by an order of magnitude

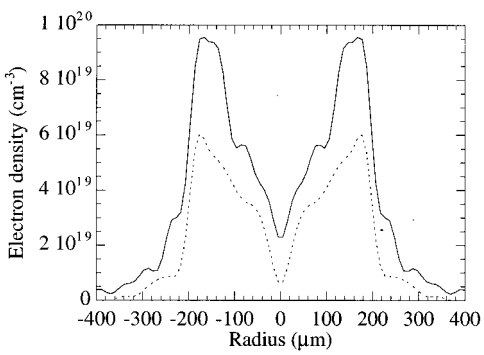

FIG. 11. Electron density profile as a function of gas-jet pressure ($E=25$ J) with $n_{at}=3\times10^{19}$ atoms/cm^3 (solid line) and $n_{at}=1.5\times10^{19}$ atoms/cm^3 (dotted line).

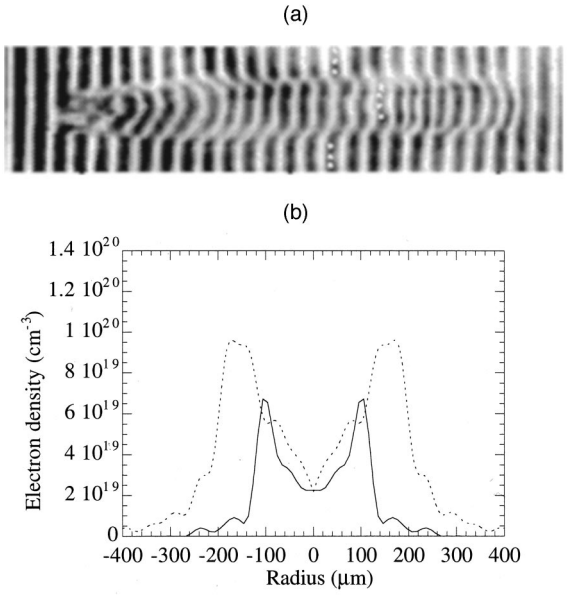

FIG. 12. (a) Time-integrated interferogram in the gas jet ($n_{at}\sim3\times10^{19}$ atoms/cm^3) for a pulse energy $E=3.5$ J ($I_{L\text{vacuum}}=7\times10^{14}$ W/cm^2). (b) Electron density profile obtained from interferograms of Fig. 4(a) and (a) of this figure. $E=3.5$ J (solid line) and $E=25$ J (dotted line).

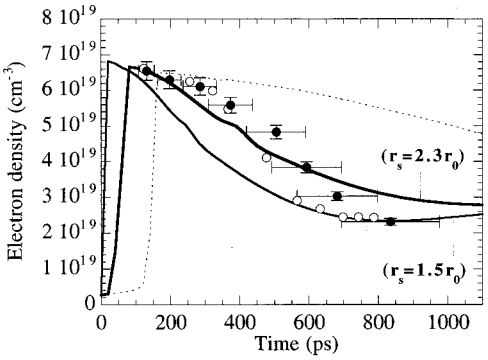

FIG. 13. Electron density evolution in the gas jet. Circles: e lectron density deduced from Fig. 6 with the Bohm-Gross relation, taking into account the thermal correction. These two shots correspond to the most different density evolutions observed experimentally. Solid line: electron density given by the simulation for our experimental parameters and a focal spot size $r_s=1.5r_0$ and $r_s=2.3r_0$. Dotted line: $r_s=7.3r_0$; r_0 and r_s are, respectively, the radius of the focal spot in vacuum and the input radius in the simulation.

(not presented in the figure) does not significantly affect the density depletion on axis. This explains why plasma channels are formed in the gas jet, even at low energy, while they are not observed in the case of gas-filled chambers where ionization-induced refraction significantly increases the laser spot size.

From the time-resolved Schlieren images, such as shown in Fig. 5(c), we measure the evolution of the position of the peak of the electron density gradient in the plasma. A comparison of the experimental data with the corresponding MULTI simulation results is shown in Fig. 14. As the probe pulse duration is 600 ps, the experimental expansion in Fig. 14 has been obtained from shots with two different delays between the pump and probe beams. These curves show that the expansion front associated with the plasma-gas interface and the corresponding electron density gradient is fast and of the order of 10^7 cm/s during the first 200 ps. This is a supersonic motion even with respect to the sound speed associated with the highest temperature usually measured ($T_{\max}$ <250 eV). A rapid decrease in the expansion rate is seen to occur 100 ps after the maximum of the interaction pulse,

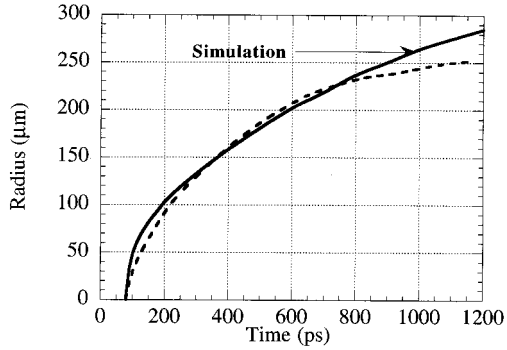

FIG. 14. Position of the gas-plasma interface as a function of time (gas jet case: $E=25$ J, $n_{\rm at}\sim 3\times10^{19}$ atoms/cm^3): experiment (dotted line) and simulation (solid line) with $r_s=2.3r_0$.

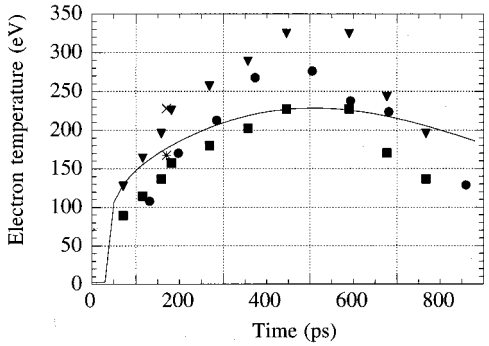

FIG. 15. Summary of experimental electron temperatures ($E=25$ J, $n_{\rm at}\sim 3\times10^{19}$ atoms/cm^3) and comparison with simulation results (solid line). The experimental temperature deduced from Fig. 7 is calculated for two cases: $T_e/T_i=1$ (triangle) and $T_e/T_i=3.5$ (square). The temperature deduced from the ratio between the ion and electron satellites of Fig. 6(a) is plotted in dots. The temperature deduced from Raman backscattering is plotted for a Landau cutoff value of $k_p\lambda_d=0.3$ (star) and $k_p\lambda_d=0.35$ (cross).

where the radial expansion velocity is reduced from 1.5×10^7 to 5×10^6 cm/s. This behavior will be discussed in the next section, Sec. IV C, on the physical processes governing the channel expansion.

The experimental and numerical values of the electron temperature are plotted in Fig. 15. As explained in Sec. II, considering the ion acoustic frequency $\omega_{\rm ia}$ given by [20]

$$\omega_{\rm ia}=2\omega_0\left[\left(1-\frac{n_e}{n_c}\right)\left(\frac{Z^*T_e/(1+k^2\lambda_D^2)+3T_i}{Am_pc^2}\right)\right]^{1/2},$$

where A is atomic number, m_p the proton mass, c the speed of light, Z^* the average ionization state, and n_e and n_c the electron and critical densities, respectively, we can deduce an upper and a lower limit for the electron temperature by fixing the ratio T_e/T_i. These two limits are in good agreement with the temperature deduced from the ratio between the ion and electron satellites of Fig. 6. Within the uncertainty of the measured temperature, we also observe good agreement with the simulation: the temperature follows the laser pulse shape and reaches a maximum close to 250 eV, 100 ps before the peak of the pulse. The fact that the temperature follows the laser pulse shape is consistent with inverse bremsstrahlung being the main heating mechanism. The fact that the maximum occurs before the peak of the pulse is explained by the decrease of electron density, which induces a decrease of the collisional absorption, sufficient to reduce the temperature before the maximum laser intensity is reached. A small discrepancy is observed near the end of the interaction where the experimental value of T_e decreases more rapidly than in the simulations. This could explain the discrepancies observed in Fig. 14 of stagnation of the channel expansion compared to simulation.

C. Discussion

Our simulations with both codes show evidence that the radial expansion of the electronic density gradient is due to an electronic heat wave driven by the collisionally absorbed

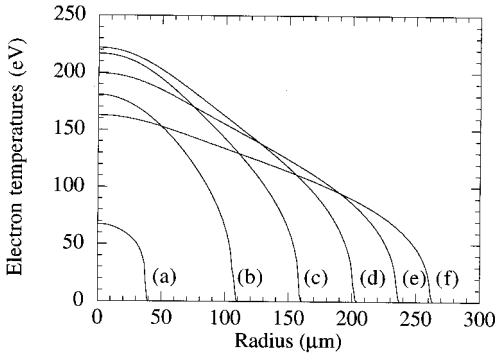

FIG. 16. Radial temperature profiles obtained in the simulation ($E=25$ J and $r_s=2.3r_0$) for (a) 10 ps, (b) 200 ps, (c) 400 ps, (d) 600 ps, (e) 800 ps, and (f) 1 ns (the maximum of the pulse is positioned at $t=600$ ps). In the time interval 0–200 ps, the speed of the thermal front is of the order of 5×10^7 cm/s and thus considerably higher than the sound speed, which is of the order of $\sim10^7$ cm/s. Later, in the interval 0.8–1 ns, the speed of the thermal front has decreased to values ($\approx10^7$ cm/s) similar to the sound speed.

laser flux. The energy deposition takes place around the axis within a radius corresponding to that of the laser beam. For times $t>100$ ps, the radius of the front of the plasma-gas interface is already considerably larger than that of the beam. The cylinder surface of the heated plasma tends to become small compared with that of the heat front so that self-similar solutions apply [26]. Anisimov [27] found that above a certain flux the corresponding solution is associated with a supersonically propagating electronic heat wave expanding with $r_h(t)\sim t^{1/2}$ into the unperturbed material, i.e., the cold gas, surrounding the heat source (r_h being the radial position of the heat front). At lower driving fluxes, as seen in some experiments [7,9,10], the governing expansion is a shock wave when the heat source is too weak to drive a supersonic heat front.

The parameters of the current experiment correspond to the electronic heat-wave case. The good agreement between the experimentally observed interface and the simulations (see Fig. 14) indeed confirms this interpretation. Figure 16 displays the electron temperature profiles obtained by MULTI simulations; the fact that the time intervals shown are equally spaced, $dt=200$ ps, illustrates that the speed of the heat front, v_h, slows down after the strong heating occurring during the rising laser pulse is finished for $t>400$ ps, i.e., $v_h(t)=dr_h/dt\sim t^{-1/2}$. Later, about $t>1.5$ ns, the speed of the heat wave drops below the sound speed and the simultaneously existing shock wave takes over to become the governing expansion mechanism.

The hydrodynamic motion behind the heat-wave front, however, happens on the acoustic time scale. Both the simulations [see Fig. 17(a)] and the density profiles deduced from the experiments [see Fig. 17(b)] show that in the course of time a ''concave'' radial density profile forms with density maxima larger than the initial density n_0 [here, in Fig. 17(a), 6.5×10^{19} cm^{-3}] close to the heat front and a minimum below the initial density n_0 at $r=0$. We see a typical density difference of 20%–25% between the axis and a radius of about 100 μm. Self-guiding effects are shown in Fig. 18, using the ray-tracing module of the FCI2 code. It is seen that

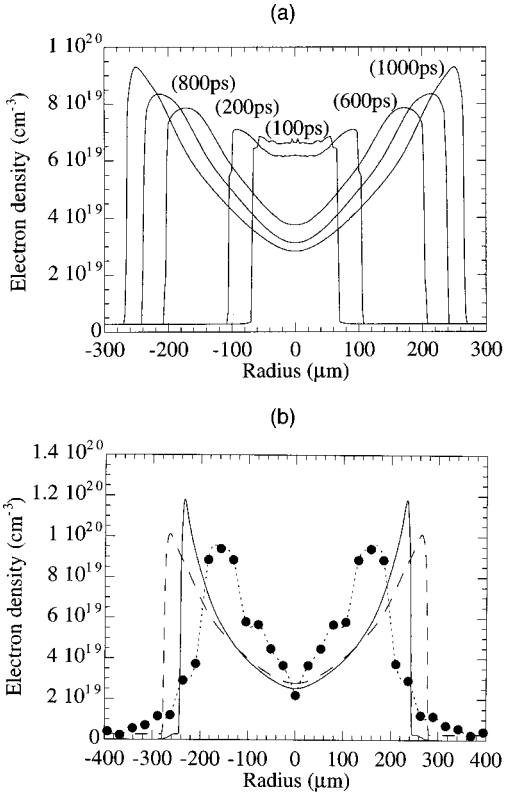

FIG. 17. (a) Channel formation in the simulation for $E=25$ J and $r_s=2.3r_0$. The different curves correspond to successive times: $t_1=100$ ps, $t_2=200$ ps, $t_3=600$ ps, $t_4=800$ ps, and $t_5=1$ ns. (b) Comparison between experimental and simulated electron density profiles. Experiment: fringe No. 20 of Fig. 4(a) (dots). Simulation: $E=25$ J, $n_{at}\approx3\times10^{19}$ atoms/cm^3 with radius $r_s=1.5r_0$ (solid line) and $r_s=2.3r_0$ (dashed line).

a significant fraction of the light beams does not diverge, but stays within a radius $r<200$ μm along the laser propagation axis (note that rays closer to $r=0$ have a higher flux than outerbound rays).

V. CONCLUSIONS

The results presented in this paper concern the formation and characterization of a plasma channel produced by the

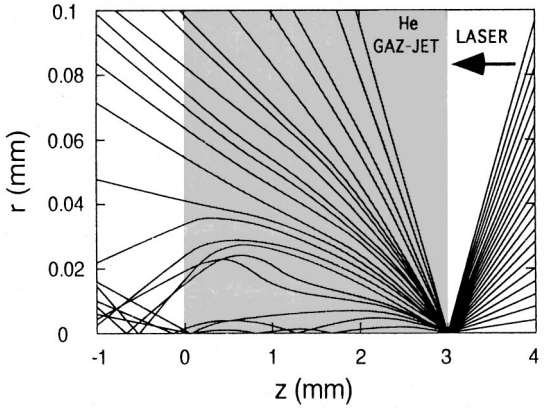

FIG. 18. FCI2 hydrosimulation of the interaction of a 600 ps laser beam with a 3 mm helium gas jet: snapshot of ray trajectories taken 200 ps before the pulse maximum shows a trapping effect. For clarity, only a few rays (1 out of 20) have been drawn.

interaction of a 600 ps laser beam with a helium gas jet. Radial electron density profiles measured by interferometry have shown an electron depletion, easily satisfying the optical guiding conditions for a second pulse, which could be focused on the edge of the gas jet, at the channel entrance. The electron density evolution along the propagation axis has been time resolved by Thomson scattering in the gas jet as well as in the gas-filled chamber. The comparison between these two cases has shown that the use of the gas jet efficiently limits the refraction of the interaction pulse, giving a spot size radius in the plasma sufficiently small to create the channel. The radial expansion is also time resolved, and Thomson scattering off electron waves and ion acoustic waves has provided electron temperature measurements. These measurements are in good agreement with simulations which indicate that the electron density channel is induced by the hydrodynamic motion behind an electron heat wave. The presented scheme appears to be a very flexible method to produce channels. It does not require high-intensity laser pulses as for relativistic self-guiding schemes and offers good control of the electron density by changing the laser energy and gas-jet pressure. Furthermore, the complete ionization of helium prevents any ionization-induced refraction of the guided pulse. The use of longer gas jets promises the production of still longer channels.

ACKNOWLEDGMENTS

The authors would like to acknowledge the support of C. Coulaud and of all the technical teams of LULI. We would like to thank Z. Najmudin for fruitful discussions and K. Eidmann for the tabulated ionization data that were used in the MULTI simulations.

[1] T. Tajima and J. Dawson, Phys. Rev. Lett. **43**, 267 (1979).
[2] A. Modena *et al.*, Nature (London) **377**, 606 (1995).
[3] E. Esarey, P. Sprangle, J. Krall, and A. Ting, IEEE Trans. Plasma Sci. **24**, 252 (1996).
[4] P. B. Corkum, N. H. Burnett, and F. Brunel, Phys. Rev. Lett. **62**, 1259 (1989).
[5] X. F. Li *et al.*, Phys. Rev. A **39**, 5751 (1989).
[6] M. Tabak *et al.*, Phys. Plasmas **1**, 1626 (1994).
[7] T. R. Clark and H. M. Milchberg, Phys. Rev. Lett. **78**, 2373 (1997).
[8] S. P. Nikitin *et al.*, Opt. Lett. **22**, 1787 (1997).
[9] C. G. Durfee III and H. M. Milchberg, Phys. Rev. Lett. **71**, 2409 (1993).
[10] C. G. Durfee III, J. Lynch, and H. M. Milchberg, Phys. Rev. E **51**, 2358 (1995).
[11] A. B. Borisov *et al.*, Phys. Rev. A **45**, 5830 (1992).
[12] A. B. Borisov *et al.*, J. Opt. Soc. Am. B **11**, 1941 (1994).
[13] P. Monot *et al.*, Phys. Rev. Lett. **74**, 2953 (1995).
[14] K. Krushelnick *et al.*, Phys. Rev. Lett. **78**, 4047 (1997).
[15] Y. Ehrlich *et al.*, Phys. Rev. Lett. **77**, 4186 (1996).
[16] S. Jackel *et al.*, Opt. Lett. **20**, 1086 (1995).
[17] M. Borghesi *et al.*, Phys. Rev. E **57**, 4899 (1998).
[18] V. Malka *et al.*, Phys. Plasmas **3**, 1682 (1996).
[19] V. Malka *et al.*, Phys. Rev. Lett. **79**, 2979 (1997).
[20] J. Sheffield, *Plasma Scattering of Electromagnetic Radiation* (Academic, New York, 1975).
[21] P. Monot *et al.*, J. Opt. Soc. Am. B **9**, 1579 (1992).
[22] R. Ramis, R. Schmalz, and J. Meyer-Ter-Vehn, Comput. Phys. Commun. **49**, 475 (1988).
[23] R. Dautray and J. P. Watteau (unpublished).
[24] K. Eidmann, Laser Part. Beams **12**, 223 (1994).
[25] R. W. P. McWhirter, in *Plasmas Diagnostic Techniques*, edited by R. H. Huddlestone and S. L. Leonard (Academic, New York, 1965).
[26] Y. B. Zeldovich and Y. P. Raizer, *Physics of Shock Waves and High-Temperature Hydrodynamics Phenomena* (Academic, New York, 1967).
[27] S. I. Anisimov, JETP Lett. **12**, 287 (1970).